



# An assessment of Dungale landslide using remotely piloted aircraft system (RPAS), ground penetration radar (GPR), and Slide & RS<sup>2</sup> Softwares

Ruchika Sharma Tandon<sup>1</sup> · Vikram Gupta<sup>2</sup> · Bhimala Venkateshwarlu<sup>3</sup> · Pradeep Joshi<sup>1</sup>

Received: 1 July 2021 / Accepted: 22 March 2022 / Published online: 4 April 2022  
© The Author(s), under exclusive licence to Springer Nature B.V. 2022

## Abstract

In the present study, slope stability analysis was done using limit equilibrium method and finite element method of the Dungale landslide situated in the NW Himalaya along Tons river. The data used for slope stability analysis was collected through geological and geotechnical field and laboratory-based studies. The field study includes remotely piloted aircraft system and ground penetration radar surveys, whereas laboratory study includes determination of engineering properties of slope forming material using standard methods. A road cut across the landslide often gets blocked during monsoon due to landslide reactivation. A fault has been identified running across the landslide at a height of ~76 m above the road from where continuous water flow is noticed, and above which instability occurred. The laboratory data reveals that the soil collected from the top of the landslide site is impermeable in nature and thus, may not uphold the flow of water into deeper horizons. Based on our investigation, we conclude that the landslide occurred in two phases. In the first phase, there is development and opening of the cracks in the uppermost layer of the soil at the top of the slope. Due to highly impermeable nature of the slope material, the upper topmost layer becomes saturated in the monsoon, and the inner layer within is dry. The differential water content exerts pressure within the soil and causes the opening of the cracks. In the second phase, the excessive flow of underground water during monsoon along the fault plane erodes the material at rock-soil interface causing the failure of the material. The slope stability analysis also confirms the limiting factors of safety during unsaturated state of soil, which lowers during saturated conditions.

**Keywords** Dungale landslide · Remotely piloted aircraft system (RPAS)/unmanned aerial vehicle (UAV) · Limit equilibrium method (LEM) · Finite element method (FEM) · Ground-penetrating radar (GPR) · Geotechnical properties · Himalaya

---

✉ Ruchika Sharma Tandon  
ruchika\_ddn@yahoo.co.in

<sup>1</sup> Graphic Era Deemed to be University, Dehradun, Uttarakhand 248 002, India

<sup>2</sup> Wadia Institute of Himalayan Geology, Dehradun, Uttarakhand 248 001, India

<sup>3</sup> USDMA, Uttarakhand Disaster Recovery Project, Dehradun, Uttarakhand, India

## 1 Introduction

Landslide activities are the frequent, widespread, and recurring phenomena in the mountainous region. These are generally caused by the downward and outward movement of the slope forming materials, mainly constituting rock boulders, soil, artificial fills, or debris. There are number of causes that contribute to the development of landslides. These are mainly the weak geological setup, critical disposition of joints, unfavorable geomorphological characteristics of slopes, and anthropogenic activities in the sensitive hilly terrains. However, rainfall and earthquakes are commonly the main triggers. Landslides are generally developed on the slopes when the pre-existing landslide conditioning factors become conducive and subsequently these are caused by any of the triggering factors.

The Himalayan mountain belt resulting from continental-continental collision of the Indian and Tibetan lithospheric plates during ~55 million years ago (Wadia 1953; Gansser 1964; Dewey and Burke 1973; LeFort 1975; Yin 2006; Jain et al. 2012) is positioned between India and China in the South Central Asia. It is believed to be still active and due to ongoing northward drifting of Indian plate below Tibetan plate, a variety of sedimentary, metamorphic and igneous rocks are exposed in the Himalaya which is extensively fractured, folded, faulted, and thrust. These rocks are divisible into Trans Himalaya, Tethyan Himalaya, Higher Himalaya, Lesser Himalaya, and Sub Himalaya which are separated from each other by major thrusts.

Landslide activities in the Himalaya are relatively common owing to variety of reasons, like frequent cloudburst events leading to abnormal and concentrated rainfall in a particular region, presence of tectonic zones that weaken the strength of the geological material, high variations in day-night temperature leading to freeze-thaw action, climatic shifting that disturb the highly populated slopes and increasing anthropogenic activities such as unplanned construction, expansion of road networks, development of large numbers of hydroelectric and tunnel projects, etc. (Sati et al. 1998; Haigh and Rawat 2011; Sarkar et al. 2012; Singh et al. 2014, Sarkar et al. 2015, Buragohain et al. 2016, Gupta et al. 2016a, b, Kundu et al. 2016; Sumantra and Raghunath 2016; Dudeja et al. 2017; Kundu et al. 2017; Sarkar and Samanta 2017; Siddique et al. 2017a, b; Singh et al. 2017; Umrao et al. 2017; Tandon et al. 2021). These landslides are primary as well as secondary in nature and cause enormous damage when associated with cloud burst activities. For example—2 major landslide events on 12th and 19th August 1998 in the Ukhimath region of Higher Himalaya completely destroyed 2 villages, killing > 100 humans & 422 cattles, and the total loss to the property was estimated ~\$0.55 million USD (Pande 2006). Another disastrous landslide occurred in the Kali river valley on 18th August 1998 in which the entire Malpa village was washed away causing > 200 fatalities. Another event on 23rd September 2003 at Uttarkashi township caused huge loss of properties and destroyed the residential and commercial establishments at the foot of the hill (Sarkar et al. 2011). Further, the intense and continuous rainfall for > 24 h in the Mandakini and adjacent valleys in the Higher Himalaya during June 2013 induced Chorabari lake outburst that accelerated thousands of the landslides, wiping out many villages, roads, and bridges and also caused > 5000 death (Ray et al. 2016). Besides, numerous small-scale landslides are very common in the entire Himalaya and frequently cause disruption to traffic during almost every monsoon season.

In order to overcome the effect of such calamities and to reduce the impact of landslides on society, it is utmost important to study and understand the causes of a particular landslide so that successful execution of mitigation works can be performed. It has been observed that most of the time, the landslides in the Himalayan terrain are controlled unscientifically

without understanding its causal factors. Improper mitigation measures always lead to failure and enhance the risk. Therefore it became a challenging task to the engineers and geoscientists to design an appropriate remedial or preventive measure using the latest technological intervention.

There are various geophysical and remote sensing techniques which are being used to obtain numerous landslide-related parameters including subsurface data like structure and depth of rock-soil interface, water table, and the spatial and temporal distribution of landslides in a region. These are subsequently used in slope stability analysis to understand the stress distribution and landslide kinematics. Among the various geophysical techniques, seismic refraction, resistivity, and ground penetration radar (GPR) are frequently being utilized for investigating the landslides (Bogoslovsky and Ogilvy 1977; Travelletti and Malet 2012; Travelletti et al. 2013; Pazzi et al. 2018, 2019; Tandon et al. 2021). GPR among the other geophysical techniques is quite accurate, cost-effective, and less time-consuming. However, it only provides information of shallower depth and thus, cannot be adopted for deep-seated landslides. In recent years, the Himalayan landslides have been investigated by Chaudhary et al. (2010), Gupta et al. (2016b), and Tandon et al. (2021) to find out subsurface structure using GPR. However, geophysical techniques, including the GPR, have operational limitation at many of the desired landslide sites in the Himalaya because of the topographical challenges. Therefore, various remote sensing techniques, operational from spaceborne, airborne, and ground-based platforms which have capability to acquire spatially continuous low to higher resolution satellite images (Tofani et al. 2013) have proved to be useful for landslide investigations (Delacourt et al. 2007). However, higher cost of the high-resolution satellite images and the lack of continuous time series data are the major drawbacks associated with these techniques. During the past decade, a rapid development in conventional remote sensing technique has accelerated the use of remotely piloted aircraft system (RPAS) or unmanned aerial vehicles (UAV) in landslide studies due to its low cost, high resolution, flexure survey planning, and real-time applicability (Chang-Chun et al. 2011; Eisenbeiss and Sauerbier 2011; Nex 2011; Niethammer et al. 2012; Tofani et al. 2013; Colomina and Molina 2014; Tanteri et al. 2017; Eker et al. 2018; Fiorucci et al. 2018; Giordan et al. 2018, 2020; Rossi et al. 2018; Notti et al. 2021). In addition, real-time monitoring of a particular landslide can be successfully employed by the RPAS, particularly in the vegetated or inaccessible areas where space-borne remote sensing is not much significant (Ruwaimana et al. 2018; Furukawa et al 2021).

In the present study, the Dungale landslide situated near Ichari dam along Tons river valley has been studied for detailed investigations to understand its causative factors responsible for the movement. The investigations include geological-geomorphological mapping using GPR and RPAS surveys, geotechnical characterization of the slope forming materials followed with the slope stability analysis. The slope stability was performed with limit equilibrium method (LEM) and finite element method (FEM) using Slide and RS<sup>2</sup> softwares. The results are compared with each other in order to determine the most representative values of factor of safety. The slope stability analysis using FEM and LEM techniques have been used by various workers in landslide-prone areas (Zhu et al. 2003; Chang and Huang 2005; Singh et al. 2008; Cheng et al. 2015; Siddique et al. 2017a, b; Pradhan and Siddique 2020; Tandon et al. 2021).

## 2 Study area

The study area falls in the Lesser Himalaya along the Tons river valley. The river cuts across various formations of Tethyan Himalaya, Central Himalaya, Lesser Himalaya, and Sub Himalaya before connecting to major river Yamuna at Poanta. The regional geology of the area has been significantly contributed by Gansser (1964), Valdiya (1980), Srivastava and Lakhera (2007), and Chauhan et al. (2021).

The Dungale landslide is located at longitude  $77^{\circ} 47' 42.22''$  E and latitude  $30^{\circ} 37' 41.61''$  N on the right bank of the east running narrow valley that connects with the reservoir of Ichari Dam on the Tons river (Fig. 1). At the base of this narrow valley, the Ichari

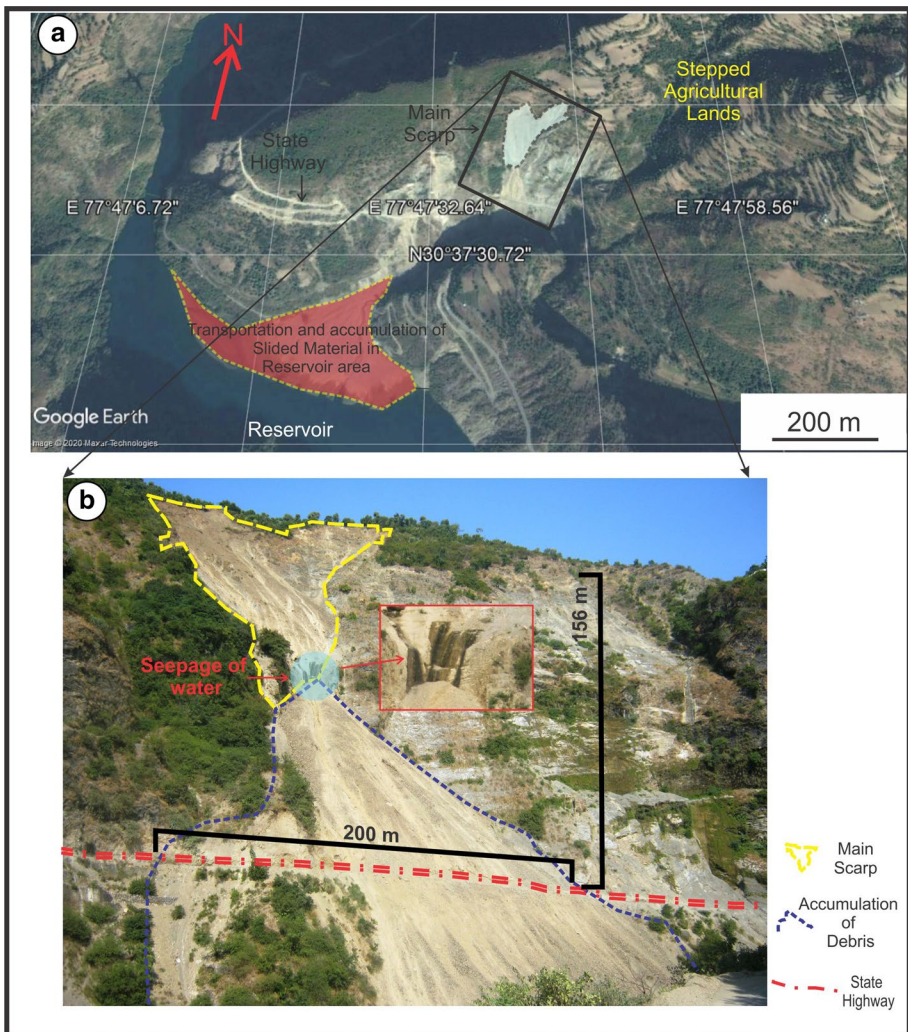


**Fig. 1** a Satellite view of Dungale landslide site showing deposition of slided material in Tons river b closure view of Dungale landslide

Gad flows whose gradient varies between  $5^{\circ}$  and  $20^{\circ}$ . A state highway which is the lifeline for the people living in the area passes through the landslide at an elevation of  $\sim 730$  m above msl (Fig. 1).

Geologically, the area is composed of thinly bedded limestone named as Bansa limestone which is bounded by the rocks of Chandpur Formation towards south and the Mandhali Formation towards north (Fig. 2a). The limestone is buff grey in color, fine to medium-grained, and gives metallic sounds on being hit by a hammer. It is thinly bedded and highly fractured (Fig. 3a) in the vicinity of the landslide. It is highly weathered towards the left side of the landslide whereas massive towards the right side of the landslide (Fig. 3b, c). The trend of the limestone is WNW- ESE dipping towards SSW with an angle of  $20\text{--}30^{\circ}$  (Fig. 3d). Numerous thin veins of calcite are present cutting across the bedding plane on the right side of landslide towards reservoir. There are three to four joint sets including the bedding joint present at the landslide site. The two prominent joint sets (J1 and J2) are sub-vertical trending  $N60^{\circ} W\text{--}S60^{\circ} E$  &  $N70^{\circ} E\text{--}S70^{\circ} W$  dipping towards  $N30^{\circ} E$  and  $N20^{\circ} W$ , respectively and are dominantly seen at right side of landslide (Fig. 3c). At places, the bedding joint (BD) exhibits wavy appearance. Generally, these joint sets are very tight in nature and persistent but few open, non-persistent, and randomly oriented joints are present near the landslide (Fig. 3d) and allow the percolation and seepage of groundwater present at various places (Fig. 3a). The wet rock surface is commonly seen towards the left side of the landslide (Fig. 3e).

Geomorphologically, the relief of the hill slope is high ( $\sim 250$  m) and slope steepness is variable ranging between  $15$  and  $70^{\circ}$ . The upper part of slope at an elevation between 1000 and 1050 m is covered with thick soil. It has gentle slope ( $10\text{--}15^{\circ}$ ) and is mainly used for cultivation (Figs. 1a and 2b). Towards the northern side of the landslide, the slopes are covered with old landslide deposits. These deposits are characterized by smooth low rounded surfaces with moderately steep slopes. There are not any visible signatures of movement on these slopes however, the presence of numerous boulders of limestone on the slopes is indicative of rockslides/falls in the past (Fig. 3f). The movement of thin layers of rock-soil matrix along with rockfall has also been observed (Fig. 3g) just adjacent to landslide. The accumulated sediments from the hill were transported into the Ichari dam reservoir through the hydrographic network, thereby adversely affecting the life of the reservoir (Fig. 4).

### 3 Methods and materials

The study comprises both, field as well as laboratory investigations. The field study includes the collection of data in the field (i.e. geological data, joint sets data) along with the remotely piloted aircraft system (RPAS) and ground penetration radar (GPR) survey. Rocks and soil samples were collected during the fieldwork for characterizing their physical and mechanical properties. These properties were used in slope stability analysis and for the calculation of the safety factor. The representative sample of soil ( $\sim 5$  kg) from the top portion of the landslide scarp and a block sample of limestone having dimension of  $15 \times 15 \times 20$  cm from the road cut section were collected to carry out testing in the laboratory so as to obtain their engineering properties. 12–15 chunks ( $\sim 5\text{--}10$  cm thick) of limestone were also collected from the landslide debris to carry out point load test. The methodology adopted for the present study and results obtained is described in the succeeding sections.



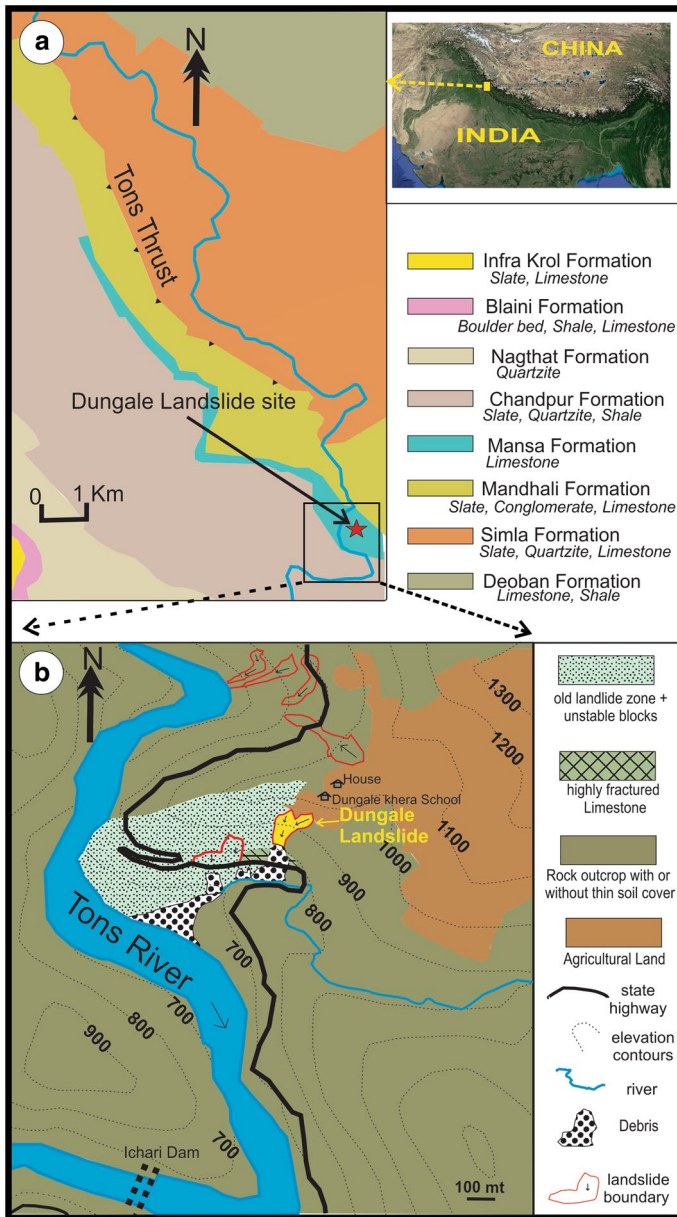


**Fig. 2** a Geological map of the study area b Geomorphological map of the Dungale landslide zone

In order to prepare the 3D model of the landslide site, the RPAS survey was performed. The RPAS or drone used in the present study is phantom professional 3 equipped with a Camera Model FC300X (focal length 3.61 mm) with resolution of 4000×3000 and 1.56×1.56 μm pixel size. High resolution point cloud of the landslide area was captured with RPAS. The RPAS was flown manually in order to cover the entire landslide site. The

images were clicked at different heights ensuring the best coverage of the target area with appropriate photo overlap. A total of 128 images were clicked from different camera stations with maximum flying altitude of 113 m and ground resolution of 2.14 cm/pix. These pictures were then processed using “Agisoft Metashape” software and 3D model and digital elevation model (DEM) of the site were constructed. It was subsequently used for the calculation of dimensional characteristics of the landslide zone. The processing of images includes—loading the photos into meta shape, aligning of photos, building of dense point cloud, building mesh (3D polygonal model), generating texture, building tiled model, digital elevation model & orthomosaic, and exporting results.

In order to decipher the subsurface structures, the ground penetration radar (GPR) survey was performed on the crown portion of the landslide (Fig. 5a) at four survey lines marked in Fig. 5b. Step frequency GPR (NGI make, model number# E5062A) has been used. It consists of two antennas i.e. transmitter & receiver (Fig. 5a), control unit, and recording unit. The central frequency of antennas was 100 MHz. The procedure involves the recording of subsurface profiles by moving the antennas along a path while maintaining a constant distance between them. During the survey, a pair of radar antennas was kept a constant offset distance of 0.75 m apart. The antennas were moved along the planned survey line with maintaining proper contact with the ground surface in order to obtain less wave’s attenuations. The parameters recorded in GPR subsurface imaging technique are the magnitude and phase (delay in two-way travel time of EM waves) of the transmitted and/or reflected electromagnetic wave.

Joints data collected from the outcrops on the right and left flank of the main landslide site (Table 1) were used for the kinematic analysis that explores the possibility of the planar and wedge failure using the software “Dips” (ver 7.014) of Rocscience. Particle size distribution, unit weight, optimum moisture content, dry density, liquid limit, plastic limit, unconfined compressive strength, cohesion, friction angle, and permeability characteristics of the collected soil samples were determined as per the Indian Standard Institution (ISI) code IS: 2720 (<https://www.services.bis.gov.in>) in the Soil Mechanics laboratory at National Geotechnical Facility (NGF), Dehradun. The results are presented in Table 2. In order to evaluate the engineering properties of limestone, the block sample was drilled into cylindrical cores having the length-diameter ratio of 2:1 and their end surfaces were smoothed and polished. These core samples were oven-dried for 24 h at ~ 105 °C before determining the various rock properties as per the standard methodologies suggested by ISRM (1981). The equations used for the measurement of density and porosity are

$$\Phi = \frac{1}{V} \left[ \frac{M_{\text{sat}} - M_s}{\rho_w} \right] \times 100 (\%) \quad \text{and} \quad \text{Density} = \frac{M_s}{V}$$

where  $V$  is the volume of the core (in  $\text{cm}^3$ ) obtained by  $V = r^2 h$  where  $r$  is radius of cylindrical core (in cm) and  $h$  is height of the core (in cm),  $\rho_w$  is the density of water,  $M_s$  is the dry mass of the core,  $M_{\text{sat}}$  is the saturated mass of the core by immersing the core sample in water for ~ 48 h.

The seismic wave velocities were determined using “Ultrasonic Pulse Transmission” (UPT) technique. There are three components i.e. pulser, transducers, and oscilloscope. In this technique, a high-energy pulser unit supplies the electric pulse which is transformed into seismic energy by a piezoelectric transmit transducer. The seismic energy travels through the whole length of the cylindrical core, placed between the transmit and the receiving transducers. The pulse was then picked by the receiving transducer which converts the seismic wave to the electrical signal and then displays it on the screen of Cathode

**Fig. 3** Field photographs depicting **a** thinly bedded limestone beds exposed in the vicinity of the Dungale landslide **b** highly weathered and leached surface of limestone exposed on the left side of the landslide **c** three sets of joints in the limestone **d** open, non-persistent vertical fracture in the limestone **e** wet slope composed of thinly bedded limestone on the left side of Dungale landslide showing development of stalagmite which is an indicator of dissolution and precipitation of calcium carbonate by groundwater **f** very large boulder of limestone lying loose on the slope **g** new landslide activity on the right side of Dungale landslide consists of varying sizes of rock-soil aggregates

Ray Oscilloscope. The initial readings of travel time were picked from the signal. Both compressional (P-) and shear (S-) wave velocities of the cylindrical cores were calculated by dividing the core length by the travel time.

The Young's modulus, a measure of the ability of a rock to withstand changes in length under compression, is the ratio of the longitudinal stress and strain. It can be static or dynamic and is obtained either from stress–strain curve of uniaxial and triaxial tests or computed from the measured wave velocities, and estimated bulk densities data. In the present study, the dynamic Young's modulus ( $E$ ) and Poisson's ratio ( $\mu$ ) of the limestone were calculated using the following equations

$$E = \left[ \rho * V_s^2 (3 V_p^2 - 4 V_s^2) \right] / (V_p^2 - V_s^2)$$

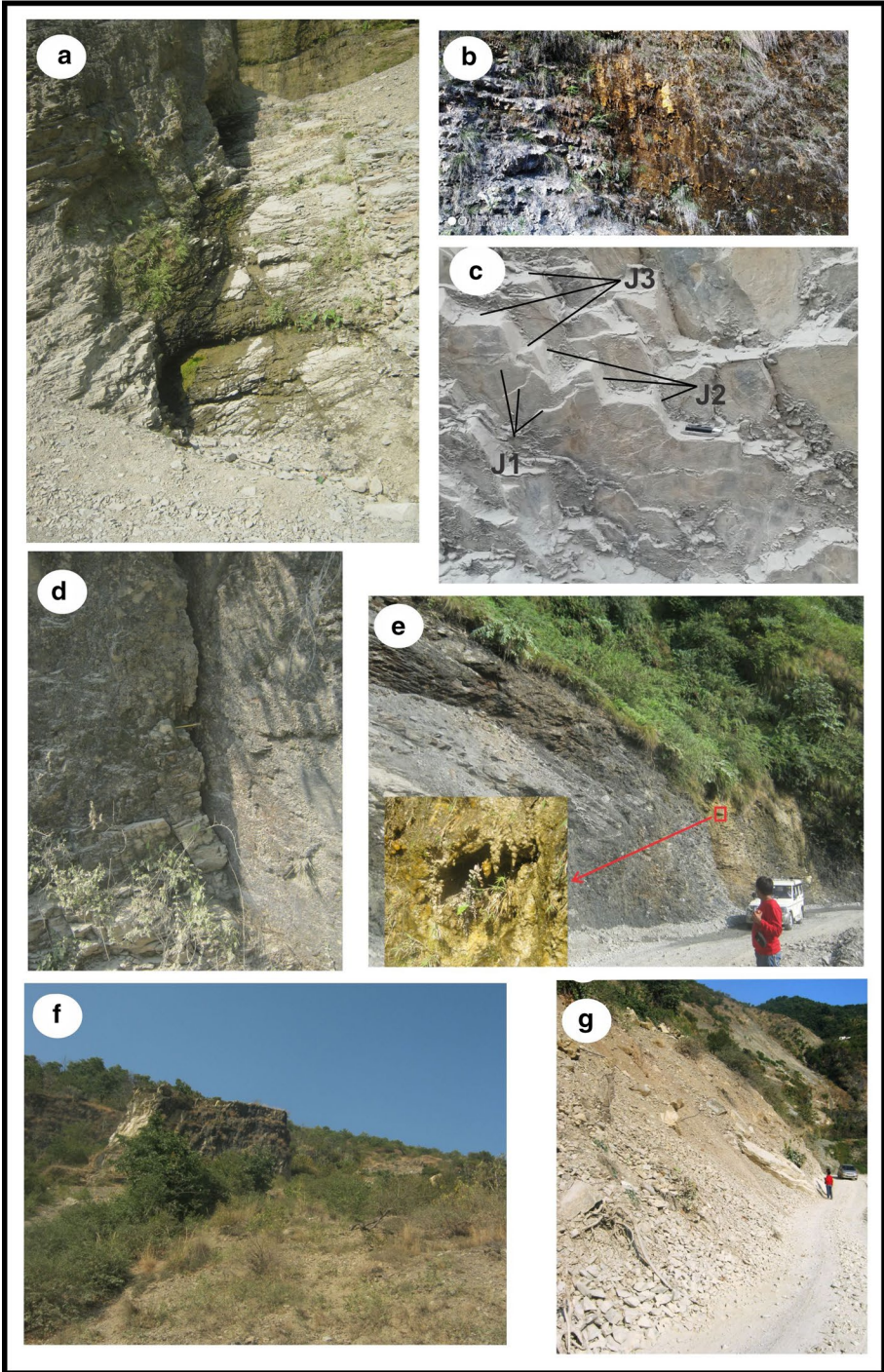
$$\mu = (V_p^2 - 2 V_s^2) / [2(V_p^2 - V_s^2)]$$

where  $V_p$  is the primary/compressional wave velocity,  $V_s$  is the shear wave velocity and  $\rho$  is the density (Table 3).

Point load tests were carried out on the lumps of limestone collected from the field. The uncorrected point load strength is calculated from the equation  $I_s = P/De^2$  where  $De$  is the equivalent diameter and calculated using the formula  $D_e^2 = 4A/\pi$  where  $A$  is the cross-sectional area of a plane between the platen contact points and calculated as product of width and diameter of each lump of rock. The size corrected point load strength ( $I_{s(50)}$ ) corresponding to a specimen of 50 mm diameter has been calculated using the equation of Brook (1985) i.e.  $I_{s(50)} = F \times I_s$ , where  $F$  is size correction factor given by  $(D_e/50)^{0.45}$ . The UCS was calculated from the equation given by Broch and Franklin (1972) i.e.  $UCS = 24 I_{s50}$  and the results are illustrated in Table 4. All these engineering properties of rock and soil were used in the slope stability analysis to assess the factor of safety (FS).

The limit equilibrium method (LEM) and finite element method (FEM) were adopted for analyzing slope stability of the landslide. The LEM is a conventional method for slope stability analysis in which slope is divided into fine slices so their base can be comparable with straight line and equilibrium equations can be derived. According to the assumptions made on the efforts between slices and equilibrium equations considered, many methods were proposed by Bishop (1955), Janbu (1957), Morgenstern and Price (1965), and Spencer (1967). However, all these methods provide similar results (Kumar et al. 2018). In the present attempt, Bishop's simplified method (Bishop 1955) has been adopted using Slide software. In this method, it is assumed that the failure surface is circular and normal interaction forces between adjacent slices are collinear and the resultant interslice shear force is zero. The factor of safety (FS) which is the ratio of the resisting forces to the sliding forces has been obtained by calculating resisting and sliding forces for each slice. The critical failure surface where the FS value is minimum among the whole analyzed surfaces was determined using the formula:-





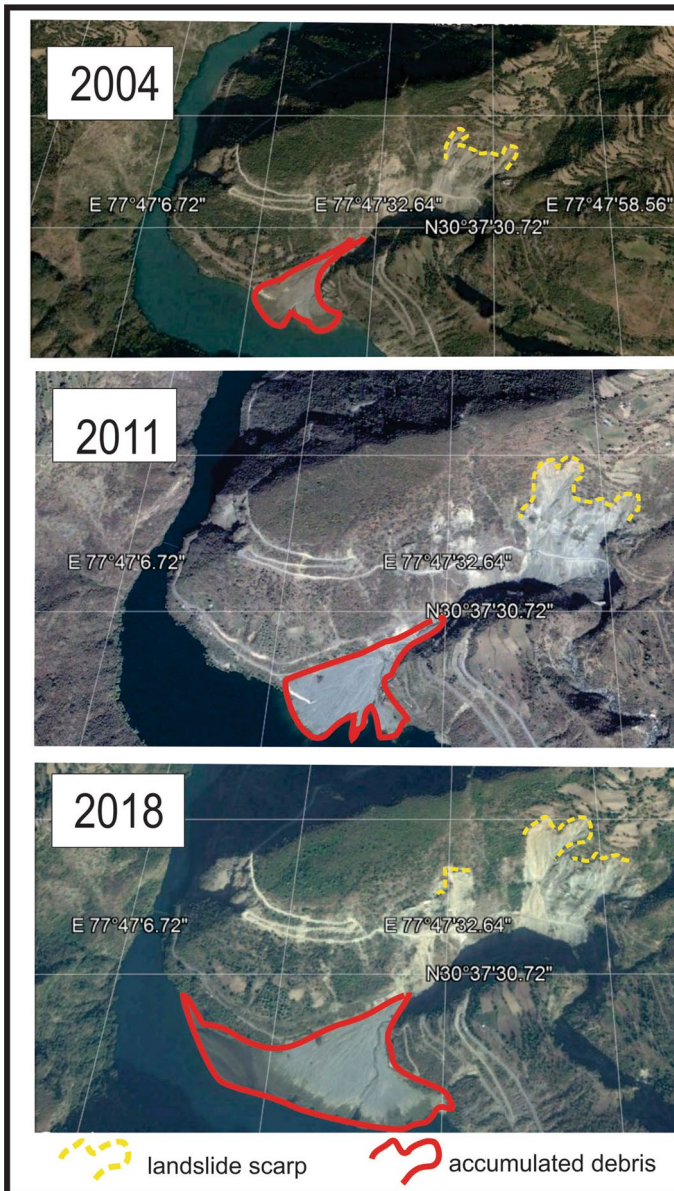


**Fig. 4** Aerial view of Dungale landslide corresponding to different years. Note the dimension of landslide scarp and volume of transported landslide material are increasing



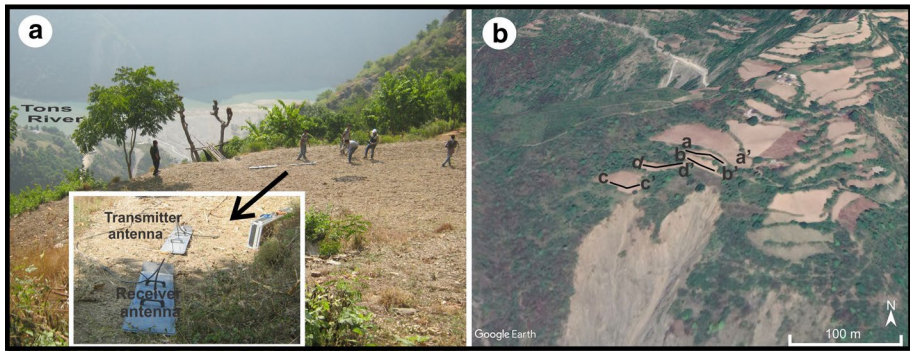


**Fig. 5** a GPR Survey over the landslide crown b lines aa', bb', cc' and dd' depicting the various transit lines for GPR survey

**Table 1** Data on the orientation of joint sets

Joint set number	Right side of Dungale landslide site		Left side of Dungale landslide site	
	Azimuth (°)	Direction (°)	Azimuth (°)	Direction (°)
BJ	30	N190	45	N70
J1	80	N290	45	N230
J2	80	N340	80	N320
J3	50	N85	–	–
Slope Face	60	N210	75	N170

**Table 2** Engineering Properties of soil collected from the top of the landslide scarp

S. No. Soil engineering properties		
1	Particle size distribution (percentage by weight of particles within different size ranges)	26.2 Gravel % 64.6 Sand % 9.2 Fines %
	Coefficient of uniformity	14.2
	Coefficient of curvature	12.8
2	Liquid limit (LL) (water content at which soil changes from plastic to a liquid state)	32.7
	Plastic limit (PL)(water content at which soil change from plastic to semi solid-state)	18.3
	Plasticity index ( difference between LL and the PL and measure of plasticity of a soil)	14.4
3	Optimum moisture content (OMC)	10.5
4	Maximum dry unit weight (MDD)	20.6 g/cc
5	Unconfined compressive strength (UCS)	100 kPa
6	Poisson ratio	0.3
7	Young modulus(E)	4.94 kPa
8	Shear parameters: cohesion (c), Friction angle (ϕ) (unsaturated)	40 kPa, 40°
	cohesion (c), Friction angle (ϕ) (saturated)	8.2 kPa, 20°
9	Permeability	10 <sup>-6</sup> –10 <sup>-7</sup>

**Table 3** Data of density, compressional & shear wave velocities, young's modulus, and Poisson's ratio on tested core samples

Sample no	Length (mm)	Diameter (mm)	Density (g/cc)	Compressional wave velocities Vp (m/s)	Shear wave velocities Vs (m/s)	Young modulus (kPa)	Poisson ratio
TVR1	64.51	37.90	2.61	3432	1988	25,738,504	0.25
TVR2	78.66	37.90	2.60	3554	2100	28,215,572	0.23
TVR3	75.21	37.90	2.68	3323	1988	25,874,080	0.22
TVR4	76.90	37.90	2.59	3476	2084	27,471,732	0.22

**Table 4** Data of point load index carried on lumps of limestone to obtain UCS values

Sample No.	Diameter			Weight			Wavg	D/W ratio	$D_e^2$	$D_e$	Cor-rection factor ( $f$ )	Failure load in kN ( $P$ ) Read- ing	Point load strength ( $I_s$ ) in kN/mm <sup>2</sup>	Point load strength index ( $I_{s(50)}$ ) in MPa	UCS = $24 * I_{s(50)}$		
	D1 (mm)	D2 (mm)	D3 (mm)	W1 (mm)	W2 (mm)	W3 (mm)											
L1	31.40	32.01	33.00	32.14	41.92	42.13	43.55	42.53	0.76	1739.66	41.71	0.92	7.20	7.23	0.00415426	3.83	<b>84.23</b>
L2	34.62	32.93	30.75	32.77	31.50	35.30	34.27	33.69	0.97	1404.98	37.48	0.88	6.80	6.83	0.00485917	4.27	<b>102.44</b>
L3	37.29	38.04	48.80	41.38	42.42	42.51	34.82	39.92	1.04	2102.06	45.85	0.96	11.20	11.23	0.00534096	5.14	<b>123.28</b>
L4	32.83	33.83	30.63	32.43	37.83	37.46	34.42	36.57	0.89	1509.41	38.85	0.89	12.80	12.83	0.00849803	7.59	<b>182.06</b>
L5	28.67	27.62	32.89	29.73	47.29	40.66	41.80	43.25	0.69	1636.32	40.45	0.91	12.90	12.93	0.00790006	7.18	<b>172.36</b>
L6	27.91	30.51	33.26	30.56	28.26	35.21	32.83	32.10	0.95	1248.51	35.33	0.86	7.80	7.83	0.00626906	5.36	<b>128.70</b>
L7	21.65	25.61	28.01	25.09	33.39	51.71	36.52	40.54	0.62	1294.55	35.98	0.86	6.10	6.13	0.00473292	4.08	<b>97.96</b>
L8	27.10	26.66	28.83	27.53	55.45	53.16	50.66	53.09	0.52	1860.18	43.13	0.94	15.70	15.73	0.00845458	7.91	<b>189.85</b>
L9	23.02	25.50	27.37	25.30	33.85	33.24	28.27	31.79	0.80	1023.40	31.99	0.82	11.00	11.03	0.01077493	8.81	<b>211.52</b>
L10	35.37	37.22	42.69	38.43	29.39	36.39	27.21	31.00	1.24	1515.94	38.94	0.89	10.70	10.73	0.00707613	6.32	<b>151.75</b>
L11	36.37	38.00	38.83	37.73	40.12	37.07	34.09	37.09	1.02	1781.38	42.21	0.93	11.20	11.23	0.00630243	5.84	<b>140.15</b>
L12	34.04	32.04	33.17	33.08	47.89	49.77	51.22	49.63	0.67	2089.58	45.71	0.96	12.00	12.03	0.0057557	5.53	<b>132.67</b>

Point load (correction factor)=0.03 kN

\*Denotes the multiplication of 24 with  $I_{s50}$



$$F = \frac{\Sigma \text{Maximum resisting forces around arc}}{\Sigma \text{Moving forces around arc}}$$

$$= \frac{\Sigma(c\Delta X + (W - u\Delta X) \tan \phi) \frac{1}{M\alpha}}{\Sigma W \sin \alpha}$$

where  $M\alpha = \frac{\cos \alpha + (\sin \alpha \tan \phi)}{F}$ ,  $W$  = weight of slice,  $X$  = normal forces, and  $E$  = tangential forces acting on boundary of slice.

The coordinates of various points of the slope were acquired from elevation profiles extracted from Google Earth Pro in order to draw geometry of landslide in slide software. The complete elevation profile from crown to toe portion of landslide was not obtained through high-resolution DEM and 3D model as we were unable to click the crown portion of the landslide site mainly due to the flight restriction in the manual mode. The total number of slices selected is 20 with maximum numbers of iteration are 50. The slope is modeled under both saturated and unsaturated conditions for soil. The properties of the slope forming material i.e. unit weight, cohesion and friction angle assigned in the model are 19 kN/m<sup>3</sup>, 40 kPa and 25° for unsaturated soil, 22 kN/m<sup>3</sup>, 8.2 kPa, and 20° for saturated soil and 25 kN/m<sup>3</sup>, 25,000 kPa and 40° for limestone. Water table was not incorporated in the model as presence of water table in the Himalaya is highly uncertain. The LEM is the most popular method for slope stability analysis but does not consider the stress–strain relationship of slope-forming material. The finite element method (FEM) is thus used generally to calculate stresses and deformational state in a soil–rock mass. The finite element method (FEM) is a numerical technique in which volume of ground is divided into simple geometric elements and the stresses and displacements compatible with the mechanical equations and the behavior law of slope forming material is considered. In our study, the shear strength reduction (SSR) method according to the Mohr–Coulomb function was adopted using RS<sup>2</sup> Software (ver. 9.030). The SSR method was proposed by Matsui and San (1992) in which the values of cohesion ( $c$ ) and internal angle of friction ( $\phi$ ) of the slope materials are reduced in steps until the soil mass fails and the critical stress reduction factor (SRF) is obtained. This critical SRF is equivalent to the factor of safety of the slope. Two geo-materials viz. soil and limestone were used in the model and the engineering properties of these i.e. unit weight, tensile strength, friction angle, cohesion, Young modulus, Poisson's ratio are 22 kN/m<sup>3</sup>, 50 kPa, 8.2 kPa, 20°, 100 MPa, 0.25 for soil and 25 kN/m<sup>3</sup>, 20 MPa, 25,000 kPa, 40°, 25 GPa, 0.27 for limestone, respectively. Fixed boundary condition has been used at the base and along the lateral sides of the model however, the slope face and the rock-debris interface were kept free for displaying displacement. The internal load applied on the model includes field stress and body forces, whereas external load is the Dungle school building located at the top of the hill.

## 4 Results

The Orthoimage, digital elevation model (DEM), and 3D construction model of the Dungle landslide site is presented in Fig. 6 obtained through processing of drone data using Agisoft Software. The images from the crown portion of the landslide, which is ~200 m above the base of the hill, could not be captured as the RPAS could fly up to maximum elevation of 110 m in manual mode and due to the fixed tilting angle of the camera lens (Fig. 6). We have measured distance between chosen referenced points like size of the boulders, retaining wall, particular rock bed, etc. on the roadside using measuring tape

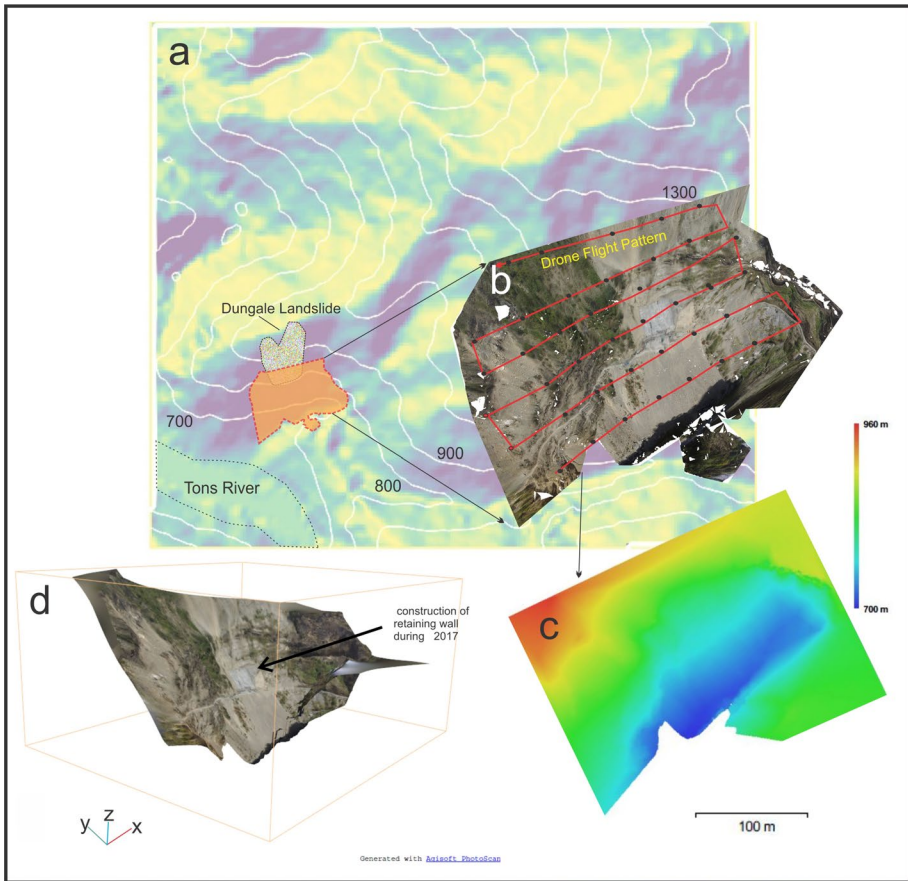


**Fig. 6** a Elevation and Hill shade map of the study area using Alos Palsar Satellite data b Orthoimage obtained during processing of drone acquired images with overlapping pattern of planned drone flight c digital terrain model and d 3D construction model of Dungale landslide site after processing the images captured by drone-Phantom Professional 3 using “Agisoft metashape”

and digital terrain model created by Agisoft and observed that the distances matches with an error of < 10 cm, however, the error using Google Earth Pro and digital terrain model is ~ 12 m. The length of the landslide along the road is measured through Google Earth Pro, DEM, and measuring tape is 207 m, 199.14 m, and 199.20 m. The 3D construction model was useful to exactly measure the various features associated with landslide with high accuracy and resolution. The drone images clearly depict the presence of joints in the middle portion of the landslide which otherwise were missed in normal view/satellite view. Further, the different type of rocks dipping in opposite direction on both sides of the landslide at a height of ~ 60 m from the road cut was observed. This might probably be due to fault passing through the area that brings the underlying orthoquartzite/quartzitic slate above the limestone.

The GPR observations allow detecting the different soil layers structures below four different elevational grounds above the crown portion of the landslide (Fig. 7). All the GPR profiles are similar in character. It has found that an upper soil layer shows higher reflectors

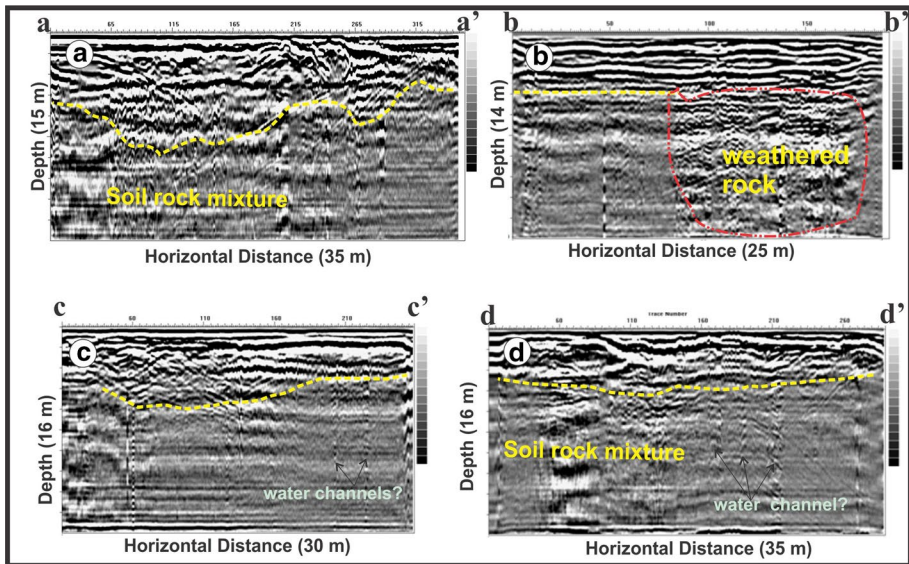


**Fig. 7** GPR reflection profile along scanned lines at four different locations present on the crown of Dungle landslide

until depth of 6–10 m and then the signal quality decreases. The yellow lines in Fig. 7 separate the upper soil to the soil-rock mixture or regolith and show the highly attenuated geomaterial below the depth of 6–10 m. It can be interpreted that the soil mixed with rock fragments is present below this depth which scatters the radar waves. The upper layer of soil is highly disturbed due to agricultural activities and considerable moist in nature. The lower soil is compact in nature and does not allow water to flow inside and hence attenuates the radar waves. The scattering of data can be seen as further below the soil layers. The scattering in GPR profile considerably reduces the amplitude of radar signals and increased the noise. No bedrock is observed upto the entire depth of radar cross-section in all four profiles which are well correlated with the field data as depth of rock bed is 50 m below the ground as seen through the road site. The vertical high reflector signal can be seen in cross-section cc' and dd' and may be interpreted as subsurface water flow channels. Since GPR profilogram exhibits the data only upto 15 m depth, that too highly attenuated and noisy, therefore information about deeper horizon and failure surface cannot be obtained using GPR studies.

The kinematic analysis reveals that there are two critical joint sets present towards the right side of landslide that allows the planar failure due to bedding joint dipping towards road and wedge failure (Fig. 8a) due to intersection of BJ with J3 and BJ with J1. This has also been evidenced in Fig. 8b in which a new landslide occurred during monsoon of 2020 located right side of the Dungle landslide and constituent of larger boundaries of limestone. The condition supported for planar failure is also attributed in Fig. 8c. The kinematic analysis further reveals that there is no chances of occurrence of planar failure towards left side of the landslide site, whereas intersection of J1 and J2 may produce wedge failure however this intersection of joints is less critical. (Fig. 8a).

The laboratory investigation of soil reveals the presence of the gravel, sand, and fine particles (silt and clay) is approximately 27%, 67.54%, and 9.2%, respectively (Fig. 9a).

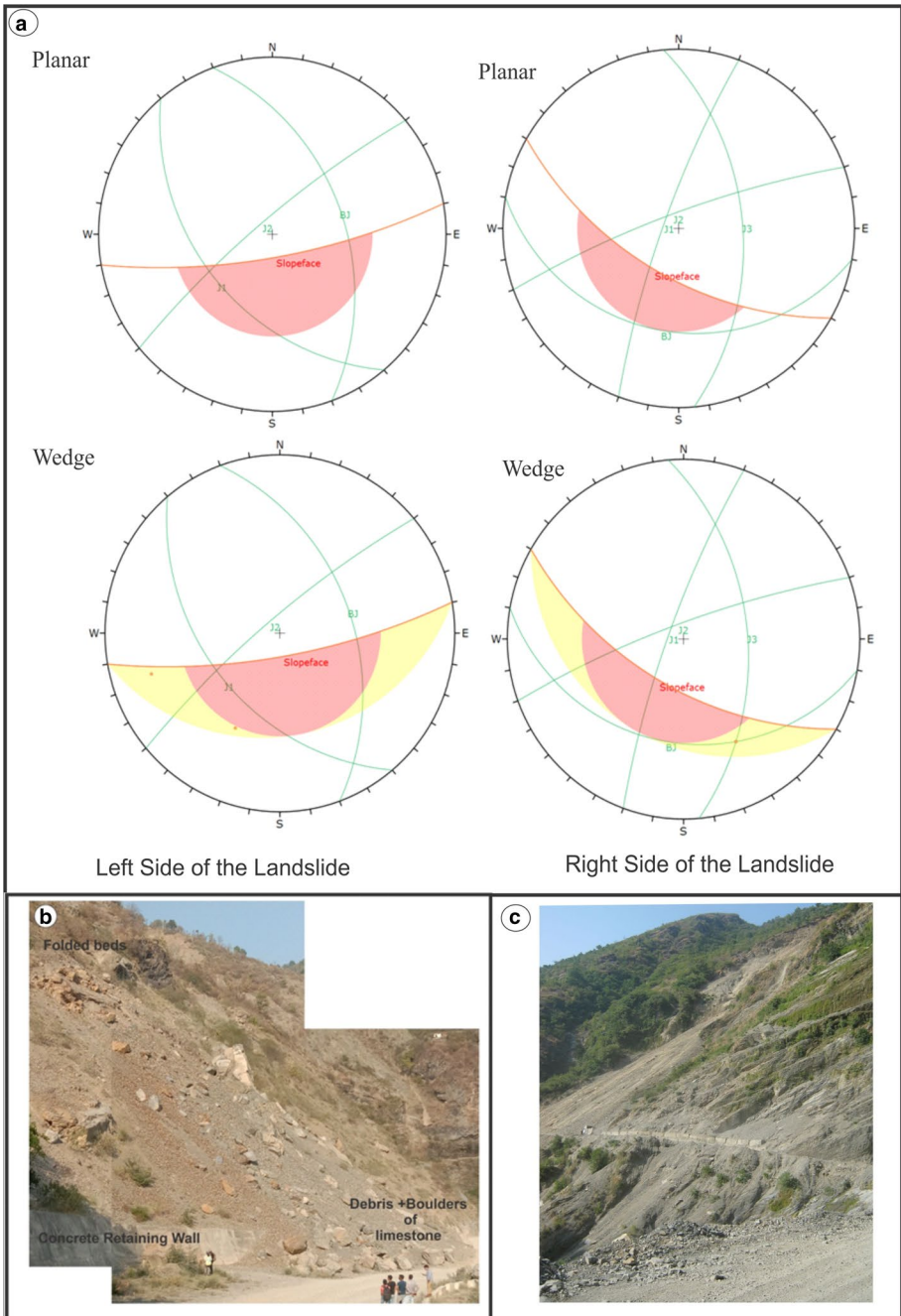


**Fig. 8** a Kinematic analysis of planar and wedge failure towards left and right of landslide scarp b picture showing the new landslide activity adjacent to the Dungale landslide on its right flank c limestone beds are dipping towards the road on right side of Dungale landslide



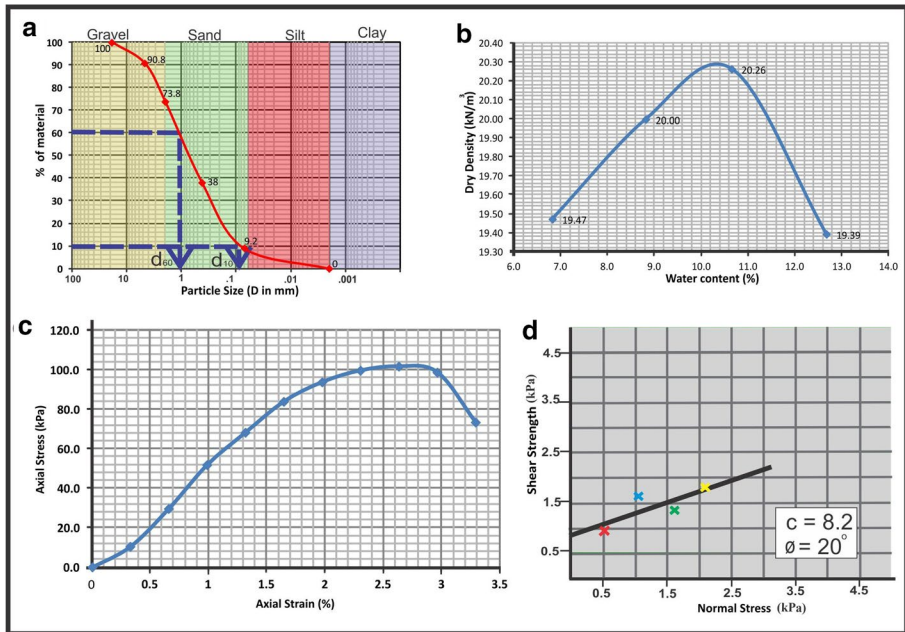


**Fig. 9** a particle size distribution in the soil collected from the top of the Dungale landslide b graph between the water content and dry density in the soil sample c graph between axial strain and axial stress obtained in unconfined compressive strength test d graph between normal and shear stress obtained in direct shear testing in order to find out c and phi in saturated condition

The coefficient of uniformity and coefficient of curvature is 14.2 and 12.8, respectively. The optimum water content (OMC) at which soil acquires the highest density is 20.30% (Table 2 and Fig. 9b). The unconfined compressive strength of the soil is 100 kPa (Fig. 9c) and angle of internal friction and cohesion are 8.2 kPa and  $20^\circ$  for saturated soil and  $40^\circ$  for unsaturated soil respectively.

The slope stability analysis depicts Factor of Safety (FS) of the landslide slope as 1.263 in the dry conditions, which reduces to 0.759 when soil is saturated (Fig. 10a, b). The critical stress reduction factor obtained from the FEM analysis is 1.2 and is in good agreement with the result obtained in LEM method (Fig. 10c). The maximum vertical displacement of ~15 cm has been observed on the top of the hill and it decreases towards the lower slope, whereas maximum horizontal displacement of ~20 cm is observed below the crown of the Dungale landslide (Figs. 10d, e).

## 5 Discussion

The RPAS/UAV has been utilized for the characterization and monitoring of landslide since last decade (Giordan et al. 2018; Rossi et al. 2018; Notti et al., 2021). Although the use of this technique in the Himalaya is very limited and still in testing mode due to highly rugged topography, very high elevations, and relief, flight restrictions, and loss of signals due to poor internet connectivity in most of the portion (Gupta et al. 2018; Watson et al. 2019). This technique allows us to obtain high-resolution orthophotos, digital surface



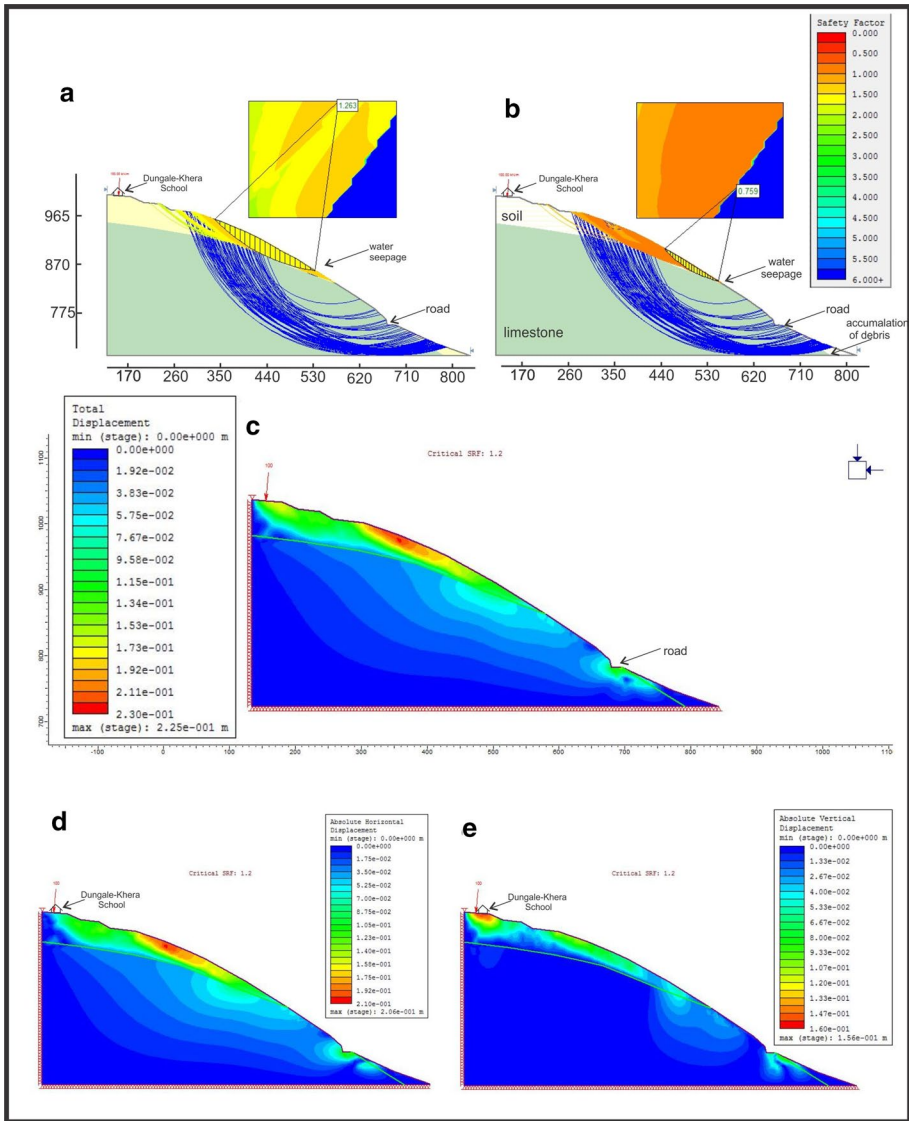


**Fig. 10** Results of slope stability analysis. Limit equilibrium analysis in **a** unsaturated soil condition, **b** saturated soil conditions using Slide software. Finite element analysis (FEM) exhibits **c** critical stress reduction factor, **d** horizontal displacement, and **e** vertical displacement using RS<sup>2</sup>software

model, and 3D view through which geomorphological mapping can be performed with high rate of accuracy (Notti et al. 2021).

In the present study, detailed geological and geotechnical studies along with RPAS/UAV and GPR studies have been carried out in and around the Dungale landslide site, where slope instability has been reported to increase in the past few years. This has been evidenced by the development of new scarps and the widening of Dungale landslide (Figs. 1, 4, and 8b). Geologically, the area is composed of limestone which is highly jointed and

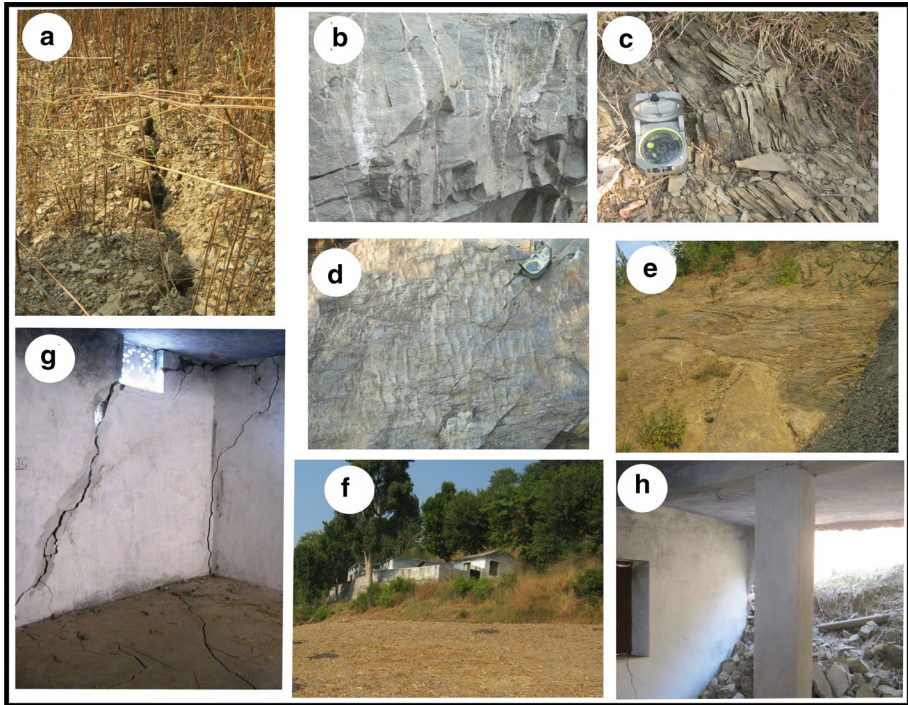


**Fig. 11** **a** Presence of tension cracks on the crown of the landslide **b** numerous vertical veins filled with secondary calcite minerals **c** folded and sheared thinly bedded slate. **d** deformed hinge portion of massive orthoquartzite in covered with ripple marks that further cuts through the slickenside **e** highly weathered and sheared rock caused due to faulting **f** view of Dungale-Khera primary school situated at the top of the Dungale hills, and **g, h** damaged walls and floor of the school building

strongly weathered in the vicinity of the landslide, whereas it is fresh and strong at far from the landslide site and thus exhibits higher compressive strength (Table 4). This weathered limestone is covered with thick overburden of soil mass on the top of the hill and has also been confirmed in the ground penetration radar (GPR) investigation. The GPR profiles reveal that the thickness of soil is  $> 16$  m on the top of the Dungale landslide (Fig. 7). A 20 m E-W trending tension crack has been observed (Fig. 11a) on the top of the hill and just above the crown of the landslide, during fieldwork in 2016 and this portion has fallen off during monsoon of 2017. Few isolated outcrops of slate and quartzites were observed on the top of the landslide towards the northern side which is highly deformed, folded & sheared and thus suggesting the tectonic activity (Fig. 11b–e). An outcrop of the orthoquartzite with slate is exposed on the top of the hill towards the north of the landslide and covered with ripple marks that further cut through the slickenside (Fig. 11d). This may probably due to the presence of fault passing through the area and have controlled the affected circulation of groundwater facilitating the landslide. Such deformed outcrops of quartzites and slate are not present on the roadside around the landslide and thus we assumed that it is buried under soil–rock matrix generated by the paleo-landslide activities. Also, a primary school is situated on the top of the hill towards north of the Dungale landslide and was packed with cracks on the walls and the floor (Figs. 11f–g). This has suggested the vertical settlement of the foundation. The collapse of the entire wall of the

school was reported (Fig. 11h) during the monsoon in 2016 after the heavy precipitation. In 2017, a concrete wall was constructed as a mitigation measures along the roadside to protect any accident at this landslide-prone site. The large portion of this retaining wall was partially buried under the debris in the next landslide event that occurred during the same year of construction. The continuous flow of underground water has been observed in the landslide area at the interface of limestone-weathered quartzitic-slate at the height of ~76 m above the road. Below this and towards left side of the landslide, the development of stalagmite in the limestone was found that suggests the groundwater dissolves the calcium carbonate and precipitated it (Fig. 3b). An open and prominent vertical joint is observed towards the left side of the landslide in which continuous water is discharging. This open vertical joint set is truncated with a fault plane that brings the underlying quartzitic slate above the limestone. The change in the thickness and direction of the bedding plane on both sides of the landslide is clearly visible in RPAS high-resolution images, which is subject to the fault activity and depicted in Fig. 12. However, fault-related structures are not visible along the roadside due to the topographical challenges and existence of wet rock surfaces which are covered with algae near the roadside (Fig. 2b). Towards the left side of the landslide and above the identified fault plane, thickly bedded rocks are noticed and well depicted in Fig. 12a. This thickly bedded rock is quartzite and quartzitic-slate and arrested in RPAS clicked pictures. The continuous water flow has been noticed



**Fig. 12** **a** Figure depicting the present of fault plane evidenced by changes in dipping direction (marked by red lines). Numerous vertical open fractures developed where seepage is commonly evidences **b** present scenario of dungale landslide. Note, the road is damaged and showing road subsidence due to clogging of water that seepage out from the landslide site. (Image clicked on April 2021)

along the fault plane in the vicinity of the landslide. Above this plane, the highly weathered rock-soil matrix is present and often falls during monsoon. The laboratory data reveals that permeability of this soil is very low in the order of  $10^{-6}$ – $10^{-7}$  (Table 2). Also, absence of any water bodies on the top of the hill affirmed that the continuous seepage of water from this part is due to the groundwater flows along the fault plane where rock is expected to be crushed and highly fractured allow easy flowage of water. The tension crack present at the top of the landslide is due to agricultural practices i.e. plowing and ripping of crops that allow rainwater to percolate into soil upto shallower depth and exert pressure due to their poor permeability and thus causes tensional cracks. The GPR investigation also reveals that there are absence of continuous rock bed upto the thickness of 16 m and radar waves get highly attenuated (Figs. 7a–d). Any soil, rocks, or sediments, which are normally dielectric (insulators), permit the penetration of radar waves without attenuation. The salinity, porosity, types of clay, and water content in soil strongly influence soil conductivity (Daniels et al. 1995; Hagrey 2000; Klotzsche et al. 2018). The carbonate minerals, sulfates, iron, salts of all sorts and charged clay particles create a highly conductive soil and readily attenuate radar energy at shallow depth (Jol 2008). Based on our investigation, we believed that the Dungale landslide occurred in two phases. In the first phase, there is development and opening of the cracks in the uppermost layer of the soil at the top of the slope. Due to highly impermeable nature of the slope material, the upper topmost layer becomes saturated in the monsoon, and the inner layer within is dry. The differential water content in the soil causes the development and the opening of the cracks in the soil. In the second phase, the excessive flow of underground water along the fault plane erodes the material at rock-soil interface, during monsoon causing the failure of the material. This has also been evidenced in the slope stability analysis which depicts that the failure surface is along the fault plane.

The stability analysis using LEM and FEM techniques reveals that under dry conditions (Fig. 10a), the soil shows a limiting value of Factor of Safety (FS) whereas it is critical under saturated conditions as water reduces shear strength of the soil (Figs. 10b, c). It was observed that water continuously flows at the soil-rock interface even though in dry season i.e. April–June although the water-flow is less. During the wet season, pore pressure at the margin of soil and limestone contact is the main reason for instability along the fault plane or soil-rock interface. The result of slope stability analysis reveals a safety factor  $> 1$  in unsaturated conditions, whereas lower (0.759) in saturated conditions close to the portion where the seepage is occurring and most similar to that is observed in the field. A similar result has also been obtained through FEM analysis using RS<sup>2</sup> Software (Fig. 10c) depicting critical stress reduction parameter of 1.2 and the high-stress distribution between the present-day crown and rock-soil interface with the maximum total displacement ( $\sim 0.80$  m) between the topographic surface and the critical failure surface. The horizontal displacements of  $\sim 0.75$  m were observed just below the crown upto soil-rock interface (Fig. 10d). The largest vertical displacements were located below the Dungale-Khera school at the top of the hill (Fig. 10e). The vertical displacement is confirmed by the presence of wide fractures on the walls and floor of the Dungale school building. Recently in 2020, stepped concrete features have been constructed at rock-soil interface from where the water is flowing. As a result, the exposed wet rock surface at the left side of the landslide became dry whereas water percolates from the base of the landslide and accumulated on the road (Fig. 12b), creating subsidence. We have observed that interrupted water flowage now moved towards the right flank of the Dungale landslide and a new landslide occurred there during 2020 (Fig. 8b).



## 6 Conclusions

Most of the landslide in the Himalaya is inaccessible due to very high relief and steep slopes, thus using UAV/RPAS could prove to be very significant. This was the first time that we have utilized Drone for the characterization and mapping of the Dungale landslide. However, since we did not have Drone data of the pre-landslide event, it was not possible to obtain relevant information about the change in geomorphology, volume, and vertical settlement of the landslide. Whereas comparing the results obtained through RPAS and from direct measurement in the field, we observed that the use of the drone for the monitoring purpose, and to obtain the vertical displacement, geomorphological and volume changes in the landslide affected area carried out pre-and post-event or before and after monsoon season can give a lot of information's about the stability conditions of the landslide and hence can be very useful for highly rugged terrain of the Himalaya. We believed that it is necessary to plan the flight in such a way to acquire entire coverage of desired area by choosing appropriate RPAS ground point.

Summing up, it has been concluded that the Dungale landslide occurred in two phases, in the first phase, there is development and opening of the cracks towards the upslope side and in the second phase, the inflow of water along the fault plane eroded the material at the soil-rock interface causing the occurrence of the Dungale landslide. Since the landslide occurred when the slope was saturated, and the strength of material reduced, therefore in order to arrest and lessen the movement, it is suggested that the percolation of water into the slope must be minimized so that there is no ingress of water into the slope. Therefore it is necessary to carry out the sub-surface investigation like resistivity survey for the determination of the depth of underground water flow.

**Acknowledgements** The authors show their gratitude to the Chancellor, Vice-Chancellor, Graphic Era Deemed to be University and the Director, Wadia Institute of Himalayan Geology, Dehradun for their support and encouragement towards research. The “National Geotechnical Facility” (NGF) under Department of Science and Technology (DST), Govt. of India is thankfully acknowledged for all the financial support to carry out field works and for providing necessary facilities. The laboratory staff of the NGF is also greatly acknowledged for the help and assistance during the laboratory testing. The anonymous reviewers are thankfully acknowledged for their constructive and insightful comments that have helped to improve the manuscript in the present form.

**Author contributions** RT contributed to Conceived the idea, collected field data, carried out drone survey along with laboratory work, and worked on the writing of the manuscript. VG Contributed towards analysis of data, development, and organization of the manuscript. BV contributed to Carried our ground penetration radar survey on the landslide site and interprets it. PJ: Contributed to the re-organization of the manuscript

**Funding** There is no funding received to carry out this research work.

**Data availability** The data and material used in this research are partly available in the body of the article; other data/material is also available to public and will be provided through writing to the author.

## Declarations

**Conflict of interest** The authors declare that they have no conflict of interest.



## References

- Bishop AW (1955) The use of the slip circle in the stability analysis of slopes. *Geotechnique* 1:17
- Bogoslovsky VA, Ogilvy AA (1977) Geophysical methods for the investigation of landslides. *Geophysics* 42(3):562–571
- Broch E, Franklin JA (1972) The point-load strength test. *Int J Rock Mech Min Sci Geomech Abstr* 9(6):669–676
- Brook N (1985) The equivalent core diameter method of size and shape correction in point load testing. *J Rock Mech Min Sci Geomech Abstr* 22:61–70
- Buragohain B, Kundu J, Sarkar K, Singh TN (2016) Stability assessment of a hill slope-an analytical and numerical approach. *Int J Earth Sci Eng* 9(3):269–273
- Chang YL, Huang TK (2005) Slope stability analysis using strength reduction technique. *J Chin Inst Eng* 28(2):231–240
- Chang-chun L, Guang-Sheng Z, Tian-jie L, A-du G (2011) Quick image-processing method of UAV without control points data in earthquake disaster area. *Trans Nonferrous Met Soc China* 21:523–528
- Chaudhary S, Gupta V, Sundriyal YP (2010) Surface and sub-surface characterization of Byung landslide in Mandakini valley Garhwal Himalaya. *Himal Geol* 31(2):125–132
- Chauhan DS, Gautam PK, Tripathy SK (2021) Structural mapping and mineral potential of Deoban group Tons valley, Kumaun Lesser Himalaya. *Himal Geol* 42(2):299–311
- Cheng YM, Li L, Liu LL (2015) Simplified approach for locating the critical probabilistic slip surface in limit equilibrium analysis. *Nat Hazards Earth Syst Sci* 15(10):2241–2256
- Cheng YM, Li L, Liu LL (2015) Simplified approach for locating the critical probabilistic slip surface in limit equilibrium analysis. *Nat Hazards Earth Syst Sci* 15(10):2241–2256
- Colomina I, Molina P (2014) Unmanned aerial systems for photogrammetry and remote sensing: a review. *ISPRS J Photogramm Remote Sens* 92:79–97
- Daniels JJ, Roberts R, Vendl M (1995) Ground penetrating radar for the detection of liquid contaminants. *J Appl Geophys* 33(1–3):195–207
- Delacourt C, Allemand P, Berthier E, Raucoules D, Casson B, Grandjean P, Pambrun C, Varel E (2007) Remote-sensing techniques for analysing landslide kinematics: a review. *Bull De La Soc Géolog De Fr* 178(2):89–100
- Dewey JF, Burke K (1973) Tibetan, Variscan and Precambrian basement reactivation: products of continental collision. *J Geol* 81:683–692
- Dudeja D, Bhatt SP, Biyani AK (2017) Stability assessment of slide zones in Lesser Himalayan part of Yamunotri pilgrimage route, Uttarakhand. *India Environ Earth Sci* 76(1):2–18
- Eisenbeiss H, Sauerbier M (2011) Investigation of UAV systems and flight modes for photogrammetric applications. *Photogram Rec* 26(136):400–421
- Eker R, Aydın A, Hübl J (2018) Unmanned aerial vehicle (UAV)-based monitoring of a landslide: Gallenzerkogel landslide (Ybbs-Lower Austria) case study. *Environ Monit Assess* 190(1):1–4
- Fiorucci F, Giordan D, Santangelo M, Dutto F, Rossi M, Guzzetti F (2018) Criteria for the optimal selection of remote sensing optical images to map event landslides. *Nat Hazard* 18(1):405–417
- Furukawa F, Laneng LA, Ando H, Yoshimura N, Kaneko M, Morimoto J (2021) Comparison of RGB and multispectral unmanned aerial vehicle for monitoring vegetation coverage changes on a landslide area. *Drones* 5(3):97
- Gansser A (1964) *The geology of the Himalayas*. Wiley, New York, p 123
- Giordan D, Hayakawa Y, Nex F, Remondino F, Tarolli P (2018) The use of remotely piloted aircraft systems (RPAS) for natural hazards monitoring and management. *Nat Hazard* 18(4):1079–1096
- Giordan D, Adams MS, Aicardi I, Alicandro M, Allasia P, Baldo M, De Berardinis P, Dominici D, Godone D, Hobbs P, Lechner V (2020) The use of unmanned aerial vehicles (UAVs) for engineering geology applications. *Bull Eng Geol Env* 79(7):3437–3481
- Gupta SK, Shukla DP (2018) Application of drone for landslide mapping, dimension estimation and its 3D reconstruction. *J Indian Soc Remote Sens* 46(6):903–914
- Gupta V, Bhasin RK, Kaynia AM, Kumar V, Saini AS, Tandon RS, Pabst T (2016a) Finite element analysis of failed slope by shear strength reduction technique: a case study for Surabhi resort landslide, Mussoorie township, Garhwal Himalaya. *Geomat Nat Hazards Risk* 7(5):1677–1690
- Gupta V, Bhasin RK, Kaynia AM, Tandon RS, Venkateshwarlu B (2016b) Landslide hazard in the Nainital township, Kumaun Himalaya, India: the case of September 2014 Balia Nala landslide. *Nat Hazards* 80(2):863–877
- Hagrey A (2000) GPR study of pore water content and salinity in sand. *Geophys Prospect* 48(1):63–85
- Haigh M, Rawat JS (2011) Landslide causes: human impacts on a Himalayan landslide swarm. *Belgeo* 3–4:201–220

- ISRM (1981). In: Brown ET (ed) Rock characterization, testing and monitoring: ISRM suggested methods. Pergamon, New York
- Jain AK, Ahmad T, Singh S, Ghosh SK, Patel RC, Kumar R, Agarwal KK, Perumal J, Islam R, Bhargava ON (2012) Evolution of the Himalaya. *Proc Indian Natl Sci Acad* 78(3):259–275
- Janbu N (1957) Earth pressures and bearing capacity calculations by generalised procedure of slices. In: Proceedings of the 4th international conference on 'soil mechanics and foundation engineering'. London, 2, pp 207–212
- Jol HM (ed) (2008) Ground penetrating radar theory and applications. Elsevier
- Klotzsche A, Jonard F, Looms MC, Van-der-Kruk J, Huisman JA (2018) Measuring soil water content with ground penetrating radar: a decade of progress. *Vadose Zone J* 17(1):1–9
- Kumar N, Verma AK, Sardana S, Sarkar K, Singh TN (2018) Comparative analysis of limit equilibrium and numerical methods for prediction of a landslide. *Bull Eng Geol Env* 77(2):595–608
- Kundu J, Sarkar K, Singh AK (2016) Integrating structural and numerical solutions for road cut slope stability analysis—a case study, India. In: Li H et al (eds) Rock dynamics: from research to engineering. Taylor & Francis Group, London, pp 457–462
- Kundu J, Sarkar K, Tripathy A, Singh TN (2017) Qualitative stability assessment of cut slopes along the national highway-05 around Jhakri area, Himachal Pradesh. *India J Earth Syst Sci* 126:112
- Le Fort P (1975) Himalayas: the collided range, present knowledge of continental arc. *Am J Sci* 275:1–44
- Matsui T, San KC (1992) Finite element slope stability analysis by shear strength reduction technique. *Soils Found* 32(1):59–70
- Morgenstern NU, Price VE (1965) The analysis of the stability of general slip surfaces. *Geotechnique* 15(1):79–93
- Niethammer U, James MR, Rothmund S, Travelletti J, Joswig M (2012) UAV-based remote sensing of the Super-Sauze landslide: evaluation and results. *Eng Geol* 128:2–11
- Notti D, Giordan D, Cina A, Manzano A, Maschio P, Bendea IH (2021) Debris flow and rockslide analysis with advanced photogrammetry techniques based on high-resolution RPAS data. Ponte Formazza case study (NW Alps). *Remote Sens* 13(9):1797
- Pande RK (2006) Landslide problems in Uttaranchal, India: issues and challenges. *Disaster Prev Manag* 15(2):247–255
- Pazzi V, Di Filippo M, Di Nezza M, Carlà T, Bardi F, Marini F, Fontanelli K, Intrieri E, Fanti R (2018) Integrated geophysical survey in a sinkhole-prone area: microgravity, electrical resistivity tomographies and seismic noise measurements to delimit its extension. *Eng Geol* 243:282–293
- Pazzi V, Morelli S, Fanti R (2019) A review of the advantages and limitations of geophysical investigations in landslide studies. *Int J Geophys*. <https://doi.org/10.1155/2019/2983087>
- Pradhan SP, Siddique T (2020) Stability assessment of landslide-prone road cut rock slopes in Himalayan terrain: a finite element method based approach. *J Rock Mech Geotech Eng* 12(1):59–73
- Ray PC, Chattoraj SL, Bisht MPS, Kannaujia S, Pandey K, Goswami A (2016) Kedarnath disaster 2013: causes and consequences using remote sensing inputs. *Nat Hazards* 81(1):227–243
- Nex F (2011) UAV photogrammetry for mapping and 3d modeling—current status and future perspectives. *International archives of the photogrammetry, remote sensing and spatial information sciences*, 38(1/C22)
- Rossi G, Tanteri L, Tofani V, Vannocci P, Moretti S, Casagli N (2018) Multitemporal UAV surveys for landslide mapping and characterization. *Landslides* 15(5):1045–1052
- Ruwaimana M, Satyanarayana B, Otero V, M. Muslim A, Syaifiq AM, Ibrahim S, Raymaekers D, Koedam N, Dahdouh-Guebas F (2018) The advantages of using drones over space-borne imagery in the mapping of mangrove forests. *PLoS ONE* 13(7):e0200288
- Sarkar S, Samanta M (2017) Stability analysis and remedial measures of a landslip at Keifang, Mizoram—a case study. *J Geol Soc India* 89(6):697–704
- Sarkar S, Kanungo DP, Chauhan PKS (2011) Varunavat landslide disaster in Uttarkashi, Garhwal Himalaya, India. *Q J Eng Geol Hydrogeol* 44(1):17–22
- Sarkar K, Singh TN, Verma AK (2012) A numerical simulation of landslide-prone slope in Himalayan region—a case study. *Int J Arab Geosci* 5(1):73–81
- Sarkar S, Kanungo DP, Sharma S (2015) Landslide hazard assessment in the upper Alaknanda valley of Indian Himalayas. *Geomat Nat Hazards Risk* 6(4):308–325
- Sati SP, Naithani A, Rawat GS (1998) Landslides in the Garhwal Lesser Himalaya, UP. *India Environ* 18(3):149–155
- Siddique T, Pradhan SP, Vishal V, Mondal MEA, Singh TN (2017a) Stability assessment of Himalayan road cut slopes along National Highway 58. *India Environ Earth Sci* 76:759

- Siddique T, Pradhan SP, Vishal V, Mondal MEA, Singh TN (2017b) Stability assessment of Himalayan road cut slopes along National Highway 58. *India Environ Earth Sci* 76(22):759
- Singh TN, Gulati A, Dontha L, Bhardwaj V (2008) Evaluating cut slope failure by numerical analysis—a case study. *Nat Hazards* 47:263–279
- Singh R, Umrao RK, Singh TN (2014) Stability evaluation of road-cut slopes in the Lesser Himalaya of Uttarakhand, India: conventional and numerical approaches. *Bull Eng Geol Environ* 73(3):845–857
- Singh AK, Kundu J, Sarkar K (2017) Stability analysis of a recurring soil slope failure along NH-5, Himachal Himalaya, India. *Nat Hazards*. <https://doi.org/10.1007/s11069-017-3076-z>
- Spencer E (1967) A method of analysis of the stability of embankments assuming parallel inter-slice forces. *Geotechnique* 17(1):11–26
- Srivastava V, Lakhera RC (2007) Geology, structure and tectonics of the Kwanu-Shillai area, Uttaranchal-Himachal Pradesh, using remote sensing techniques. *Himalaya (geological Aspects)* 5:229–264
- Sumantra SB, Raghunath P (2016) Causes of landslides in Darjeeling Himalayas during June–July, 2015. *J Geogr Nat Disasters* 6(2):1–5. <https://doi.org/10.4172/2167-0587.1000173>
- Tandon RS, Gupta V, Venkateshwarlu B (2021) Geological, geotechnical, and GPR investigations along the Mansa Devi hill-bypass (MDHB) Road, Uttarakhand, India. *Landslides* 18(3):849–863
- Tanteri L, Rossi G, Tofani V, Vannocci P, Moretti S, Casagli N (2017) Multitemporal UAV survey for mass movement detection and monitoring. *Workshop on world landslide forum*. Springer, Cham, pp 153–161
- Tofani V, Segoni S, Agostini A, Catani F, Casagli N (2013) Use of remote sensing for landslide studies in Europe. *Nat Hazard* 13(2):299–309
- Travelletti J, Malet JP (2012) Characterization of the 3D geometry of flow-like landslides: a methodology based on the integration of heterogeneous multi-source data. *Eng Geol* 128:30–48
- Travelletti J, Malet J, Samyn K, Grandjean G, Jaboyedoff M (2013) Control of landslide retrogression by discontinuities: evidence by the integration of airborne and ground based geophysical information. *Landslides* 10(1):37–54
- Umrao RK, Singh R, Sharma LK, Singh TN (2017) Soil slope instability along a strategic road corridor in Meghalaya North-Eastern India. *Arab J Geosci* 10:260
- Valdiya KS (1980) *Geology of kumaun lesser Himalaya*. Wadia Institute of Himalayan Geology, Dehradun. p 291
- Wadia DN (1953) *Geology of India*, 3rd edn. MacMillan and Co Limited, London, p 123
- Watson CS, Kargel JS, Tiruwa B (2019) UAV-derived Himalayan topography: hazard assessments and comparison with global DEM products. *Drones* 3(1):18
- Yin A (2006) Cenozoic tectonic evolution of the Himalayan orogen as constrained by along-strike variation of structural geometry, exhumation history, and foreland sedimentation. *Earth Sci Rev* 76(1–2):1–131
- Zhu D, Lee CF, Jiang HD (2003) Generalised framework of limit equilibrium methods for slope stability analysis. *Geotechnique* 4:377–395

**Publisher's Note** Springer Nature remains neutral with regard to jurisdictional claims in published maps and institutional affiliations.